NANO LETTERS

Letter

pubs.acs.org/NanoLett

Mapping the Photoresponse of $CH_3NH_3PbI_3$ Hybrid Perovskite Thin Films at the Nanoscale

Yasemin Kutes,[†] Yuanyuan Zhou,[‡] James L. Bosse,[†] James Steffes,[†] Nitin P. Padture,[*,‡] and Bryan D. Huey[*,†]

[†]Department of Materials Science and Engineering, University of Connecticut, Storrs, Connecticut 06269, United States

[‡]School of Engineering, Brown University, Providence, Rhode Island 02912, United States

Supporting Information

ABSTRACT: Perovskite solar cells (PSCs) based on thin films of organolead trihalide perovskites (OTPs) hold unprecedented promise for low-cost, high-efficiency photovoltaics (PVs) of the future. While PV performance parameters of PSCs, such as short circuit current, open circuit voltage, and maximum power, are always measured at the macroscopic scale, it is necessary to probe such photoresponses at the nanoscale to gain key insights into the fundamental PV mechanisms and their localized dependence on the OTP thin-film microstructure. Here we use photoconductive atomic force microscopy spectroscopy to map for the first time variations of PV performance at the nanoscale for planar PSCs based on hole-transport-layer free methylammonium lead triiodide ($CH_3NH_3PbI_3$ or $MAPbI_3$) thin films. These results reveal substantial variations in the photoresponse that correlate with thin-film microstructural features such as intragrain planar defects, grains, grain boundaries, and notably also grain-aggregates. The insights gained into such microstructure-localized PV mechanisms are essential for guiding microstructural tailoring of OTP films for improved PV performance in future PSCs.

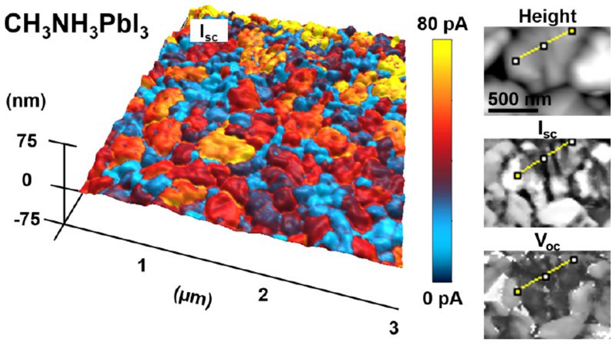

KEYWORDS: *Hybrid perovskite, photovoltaics, conductive AFM, PV performance*

Perovskite solar cells (PSCs) that use solution-processed hybrid organolead trihalide perovskites (OTPs) as thin-film light absorbers are of tremendous interest of late.[1−5] The unprecedented rise in the power conversion efficiency of PSCs from 3.8%[4] to 21%[5] within a short period of time (six years) and the promise of low-cost fabrication of PSCs is fueling this interest. The most well-studied OTP for PSCs is methylammonium lead triiodide ($CH_3NH_3PbI_3$ or $MAPbI_3$), which is relatively easy to solution-process. $MAPbI_3$ OTP thin films in planar PSCs are typically polycrystalline with average grain sizes ranging from 100 nm to a few microns.[6−8] $MAPbI_3$ belongs to a class of "soft" OTPs that have low formation energy[9] and depending on the solution-processing method used to deposit the thin films are known to have variable crystallinity and defect concentration within grains.[6,7,10−12] In fact, within the same $MAPbI_3$ thin film there can be grain-to-grain variability in crystallinity, defect concentrations, and orientation.[7,13−15] Consequently, the local properties of $MAPbI_3$ thin films are likely to be variable at the microstructure level, which in turn may influence the local photovoltaic (PV) performance parameters. However, the measurement of PV performance parameters is invariably performed at the macroscopic scale[7] on areas ranging from ∼0.1 to ∼1 cm^2, which averages the local variability in the $MAPbI_3$ properties at the microstructure level. While several scanning probe methods, such as Kelvin probe force microscopy,[7,16−18] conductive atomic force microscopy (cAFM),[18] and piezoresponse force microscopy,[19] have been used to characterize the local properties of $MAPbI_3$ thin films, direct local measurements of PV performance parameters at the nanoscale are lacking. These measurements are likely to provide key insights into the local microstructural effects on the PV performance and are essential for guiding the microstructural tailoring of OTP films for high-efficiency PSCs of the future.

In this context, photoconductive AFM spectroscopy (pcAFMs) is an ideal tool for probing local PV response at the nanoscale. The pcAFMs technique is based on AFM, and it leverages the nanoscale conductance mapping (NCM)[20] technique. NCM operates similar to continuous imaging tunneling spectroscopy,[21] where a sequence of conductive AFM images in a single region are acquired, each at a distinct voltage within a current−voltage ($I−V$) range of interest. Extended to photoconduction measurements by simultaneous specimen illumination, this approach allows the acquisition of solar-cell $I−V$ data efficiently with true nanoscale spatial resolution.[22] Here, pcAFMs is applied to planar $MAPbI_3$ OTP thin films to map for the first time the crucial photoreponse parameters, short-circuit current (I_{SC}), open-

Received: October 12, 2015
Revised: April 8, 2016
Published: April 26, 2016

DOI: 10.1021/acs.nanolett.5b04157
Nano Lett. 2016, 16, 3434−3441

circuit voltage (V_{OC}), and maximum power point (P_{MAX}), at the nanoscale, revealing profound inter- and intragranular variations in the local photoresponse of the thin films.

For the fabrication of the film sample, fluorinated tin oxide (FTO)-coated glass was patterned using HCl-(25%)-etching with Zn powder, and cleaned by soaking in a basic bath (5 wt % NaOH in ethanol) overnight. After washing with deionized water and ethanol, a compact TiO_2 electron-transport layer (ETL) was deposited on top of the patterned FTO/glass by spray pyrolysis at 450 °C. The perovskite thin film deposition method is based on procedures reported previously.[7,23] A 42 wt % precursor solution of MAI (Dyesol, Queanbeyan, Australia) and PbI_2 (Acros Organics, Pittsburgh, PA) (MAI/PbI_2 = 1:1 molar ratio) was prepared by dissolving the mixture in a mixed solvent of 1-*N*-methyl-2-pyrrolidinone/*γ*-butyrolactone (7:3 by weight). The precursor solution was then spin-coated on the compact TiO_2-coated FTO/glass at 4500 rpm for 10 s. The substrates were immediately transferred into a stirring diethyl ether (Fisher Chemical, Pittsburgh, PA) bath for 2 min. The film was then taken out and dried rapidly by using a nitrogen jet. The as-dried film was then thermally annealed at 150 °C for 5 min and it was characterized soon after.

Figure 1 is a schematic diagram showing a planar PSC mounted in a pcAFMs configuration for measuring local PV performance parameters during illumination from the bottom through the transparent-conducting cathode (FTO/glass). The compact TiO_2 serves as the ETL, and the conductive AFM probe serves as the anode. A hole-transport layer (HTL), which is typically present on top of the OTP thin film in a PSC, was not included so as to preclude obscuring any details of the localized properties of the OTP thin film. This allowed us to focus on the photoresponse of the $MAPbI_3$ thin film itself. This configuration could be considered as a HTL-free PSC with the conductive AFM probe serving as the top electrode. The displayed surface topography is a three-dimensional (3D) representation of a 3 μm × 3 μm region of the $MAPbI_3$ films, acquired by contact mode AFM.

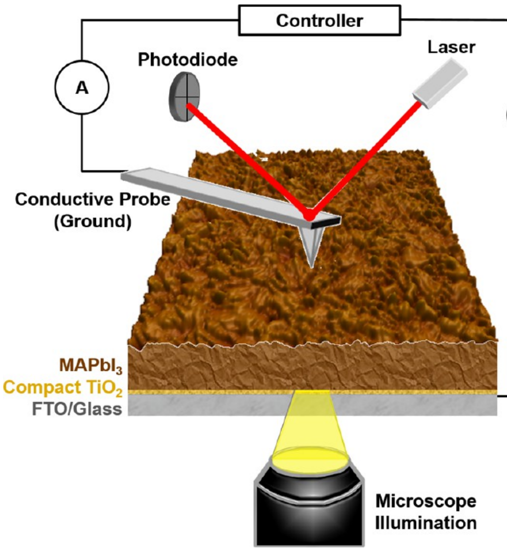

Figure 1. Schematic diagram of the pcAFMs configuration where the PSC is illuminated from below through a transparent-conducting cathode (FTO/glass) while measuring local current with a positionable conductive AFM probe anode from above. This diagram includes a 3D rendered, 3 μm × 3 μm, topographic AFM image of a $MAPbI_3$ thin film, along with a schematic cross section of the PSC containing a compact TiO_2 ETL but no HTL.

All pcAFMs measurements were performed using an MFP-3D AFM (Asylum Research, Santa Barbara, CA) operated in air. Current detection was achieved with an Asylum Research ORCA cantilever holder, providing a readout of electrical current from 20 nA down to a noise floor of ~1 pA. Conducting PtIr-coated silicon probes (Bruker, Billerica, MA) with a work function of ~5 eV, a nominal resonant frequency of 13 kHz, and a nominal spring constant of 0.2 $N.m^{-1}$ were employed for all AFM measurements. This system is mounted on an optical microscope (Nikon TE-2000, Melville, NY) with a 40× objective lens (Plan Achromat, 0.65 numeric aperture), enabling simultaneous pcAFMs imaging from the top during illumination from below through the FTO/glass cathode. The light source is a focused, unfiltered MK-R 12 V LED (CREE, Durham, NC) with an approximate illumination intensity of 0.07 $W.cm^{-2}$ (equivalent to 0.7 suns but not AM1.5G spectrum) as measured with a silicon reference cell calibrated separately with a 300 W Sol2A solar simulator (Oriel Instruments, Irvine, CA). Ambient light is minimized by experimenting in a dark room. However, a ~5 mW infrared (IR) superluminescent diode (860 nm) is used by the AFM to detect probe deflection throughout the experiments. This is not expected to influence the photoconductivity measurements, because the overhanging cantilever and probe partially shadow the interrogated region of the specimen from this continuous background of low intensity IR photons. Furthermore, the $MAPbI_3$ absorption edge is well below 860 nm.[24,25]

Figure 2a is a 3 μm × 3 μm AFM image (contact mode) showing the representative smooth surface topography for the relatively smooth $MAPbI_3$ thin film. Bright and dark contrast indicates protrusions and depressions in the range ±15 nm, respectively, revealing an overall root-mean-square (RMS) roughness of ~5 nm and grain sizes up to ~500 nm, with "wrinkled" surfaces suggesting faceting and/or intersection of planar defects (twin boundaries, stacking faults) with the surface. Figures 2b and 2c show I_{SC} contrast images of the same area (same current scale) in dark and under light respectively, showing significant differences. While the distribution of dark I_{SC} is homogeneous and essentially negligible (all < 6pA, with a mean of 0.06 pA), the illuminated I_{SC} distribution is both stronger (41.8 pA mean ranging up to 100 pA) and remarkably location-dependent and heterogeneous.

To better visualize the highly granular I_{SC} response under light, the current image of Figure 2c is overlaid on a 3D map of the topography (Figure 2d) using the same color contrast as in Figure 2c. These images (Figure 2c,d) demonstrate clearly the heterogeneity of the I_{SC} distribution across the area for the HTL-free $MAPbI_3$ film. Histograms of this photocurrent reveal that the strongest 40% of the I_{SC} values occur in less than 20% of the sampled area (Supporting Information Figure S1). While this might suggest low quality films and by extension poor performance solar cells, identical specimens fully assembled (with an HTL) into regular sized reference cells yielded efficiencies of 14.7% with J_{SC} = 20.4 mA/cm^2, V_{OC} = 1.07 V, and fill factor (FF) = 0.67.[7]

Qualitatively similar enhancements in terms of variations for grains and especially grain boundaries have been reported elsewhere.[26−30] What is especially unique to these results is that Figure 2c,d reveals interconnected aggregates of several adjacent grains, not just individual grains, exhibiting similar low (blue) or high (orange/yellow) I_{SC}. The lack of an I_{SC}

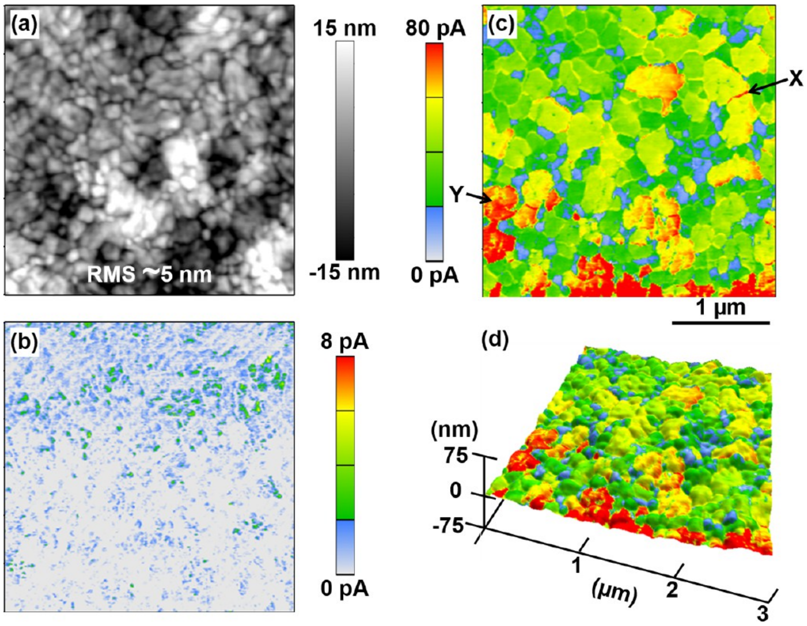

Figure 2. Two-dimensional images of 3 μm × 3 μm region of a $MAPbI_3$ thin film (same magnification): (a) topography, (b) dark I_{SC}, and (c) I_{SC} under 0.07 $W.cm^{-2}$ illumination. (d) Three-dimensional representation of the topography, overlaid by the illuminated I_{SC} color contrast collected over the same area, revealing the microstructure-specific response. Same current scale for (c,d).

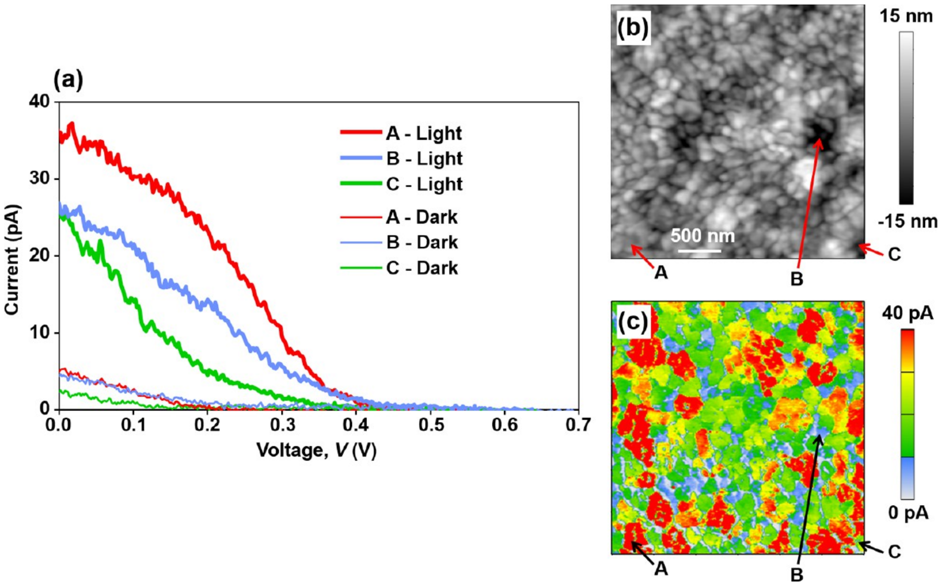

Figure 3. $MAPbI_3$ thin film (a) current measurements as a function of applied bias from +1 to 0 V in light and dark conditions for grains marked A, B and C in (b) AFM topographic image and (c) I_{SC} map of the same area.

gradient either within individual grains, or for grain-aggregates, has two implications. Photocarriers are sufficiently mobile, or electron−hole recombination is minimized, to laterally traverse at least up to ∼400 nm (the largest such features detected) without significant scattering or degradation in the carrier concentration, even across some grain boundaries.

There are several likely explanations for the observed spatial variability in I_{SC}. Given the nontextured (random) nature of the $MAPbI_3$ grains for the thin films studied here,[7] individual grains with distinct crystallographic orientations having different I_{SC} is understandable considering anisotropy in absorption, transport, and/or band alignment and is an important aspect of ongoing research. Variations in surface orientation and/or termination, local compositional changes or point defect densities,[31] or the presence of surface contaminants may also influence the detected signal especially at the tip−sample junction. But these effects would be expected within single grains, not patches of grains. Any composition or point defect gradients, changes in the surface termination (e.g., related to surface reconstructions, ionic diffusion,[32] or even ferroelectric or ferroelastic domain orientations[33−38]) should similarly be grain-orientation dependent, which will be random or even subgranular for such untextured films and therefore cannot explain the uniform supergranular responses. Contamination would likely be expected uniformly, or possibly in occasional linear streaks if caused by or spread by the rastering AFM probe, but neither are apparent.

DOI: 10.1021/acs.nanolett.5b04157
Nano Lett. 2016, 16, 3434−3441

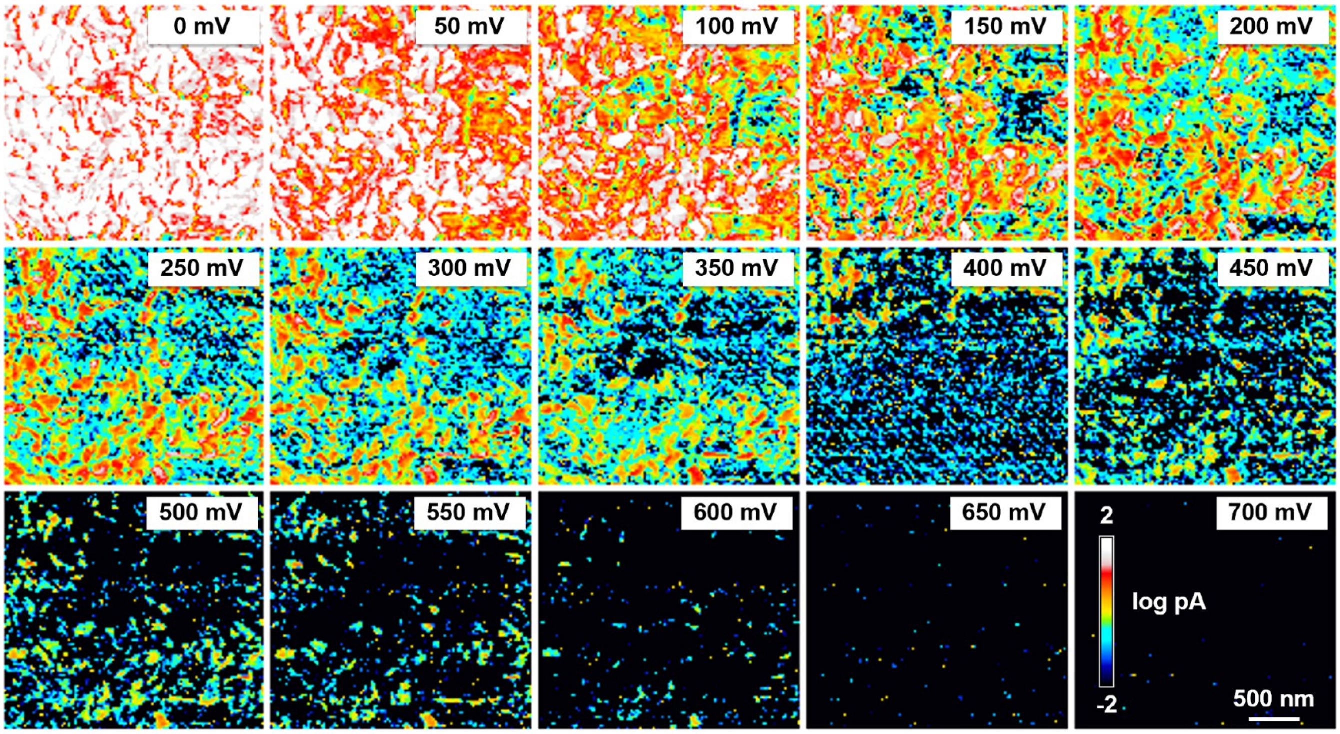

Figure 4. Montage of pcAFMs current images, all for the same 2.86 μm × 2.61 μm area during ~0.07 W.cm^{-2} illumination, but each at distinct applied voltages as labeled. Note the logarithmic current scale, representing currents from 0.01 pA (black) to 100 pA (white).

Significantly, transport is clearly hindered by certain boundaries between grains or grain-aggregates, which effectively funnels current through local high-conductivity regions comprising other interconnected grains, grain boundaries, and/or planar defects. The grain boundary identified as region X in Figure 2c is one such example with an enhanced I_{SC}, as compared to the adjacent grains exhibiting lower I_{SC}. Conversely, Region Y exhibits a lower I_{SC} compared to the surrounding area. This opposing behavior is observed despite similar topographic depressions at each location, suggesting that topography-related artifacts, which must always be considered in AFM-based measurements, are negligible in this case. Instead, some grain boundaries and/or buried interfaces simply act as effective barriers to transport. Other interfaces serve as low-resistance collectors for photocarriers generated within individual grains and/or interconnected grain-aggregates, essentially gathering photocarriers from throughout the surrounding area. This highlights an important area for future fundamental research: isolating and identifying the character, composition, and orientation of beneficial as well as detrimental current pathways in order to engineer improved performance in PSCs.

This hypothesis of a network of low- and high-conductivity channels, coupled with diffusion lengths from 100 nm[39] to 1 μm,[40] microstructure-dependent carrier mobilities,[41] and high carrier lifetimes,[42,43] is further supported by the general observation that apparently smaller grains or grain-aggregates in Figure 2c exhibit a relatively low I_{SC} response of 8–30 nA (blue). The discrete I_{SC} for larger areas rises through 30–60 pA (green/yellow), and up to 60–80 pA (orange/red) as their lateral dimensions approach ~400 nm. Thus, when the conducting AFM probe (anode) is positioned within any region of uniform but unique I_{SC}, it is likely that the measured signal represents a significant fraction of the photoconduction throughout the entire grain or grain-aggregate. This will be dictated by the local composition, optical absorption efficiency, or the surrounding interconnected low- and high-conductivity channels as demonstrated in Figure 2. Similar interpretations have been reported with macroscopic studies of specimens with varying average grain sizes.[44] Of course, the most direct path to the back electrode may be throughout the entire region of uniform contrast, or localized to a single interface. However, only full 3D photocurrent mapping at the nanoscale can answer this question, which has never before been reported.

The two-dimensionally heterogeneous photoresponse for the $MAPbI_3$ thin film is further exemplified in Figure 3 through individual $I-V$ spectra (Figure 3a) acquired for grains with distinctly different I_{SC} values: A (red), B (blue), and C (green). The locations are identified on topography (Figure 3b) and I_{SC} maps (Figure 3c), where these maps were acquired in a manner similar to that in Figure 2, but at a different location on the same sample. The $I-V$ curves were recorded by measuring the current, while sweeping the probe bias between 0 and 1 V in voltage steps of ~5.7 mV, both in dark (dotted) and under light (solid). Little variation in the dark current is observed in Figure 3a (currents below 0 pA, that is, no longer performing work, are truncated to 0), similar to what is seen in Figure 2b. Upon illumination of the $MAPbI_3$ film, though, there are substantial grain-to-grain variations not just in I_{SC} but also in the apparent V_{OC} and FF.

To map these critical PV photoresponse parameters more precisely, Figure 4 presents 15 consecutive pcAFMs current maps from a different region (2.86 μm × 2.61 μm) in the same $MAPbI_3$ thin film. All images were acquired during ~0.07 W.cm^{-2} illumination, but each at a different bias voltage, increasing between 0 and 700 mV (well beyond V_{OC}) in steps of 50 mV as indicated. Repeating each voltage condition twice, once for dark and once for light conditions, ultimately required

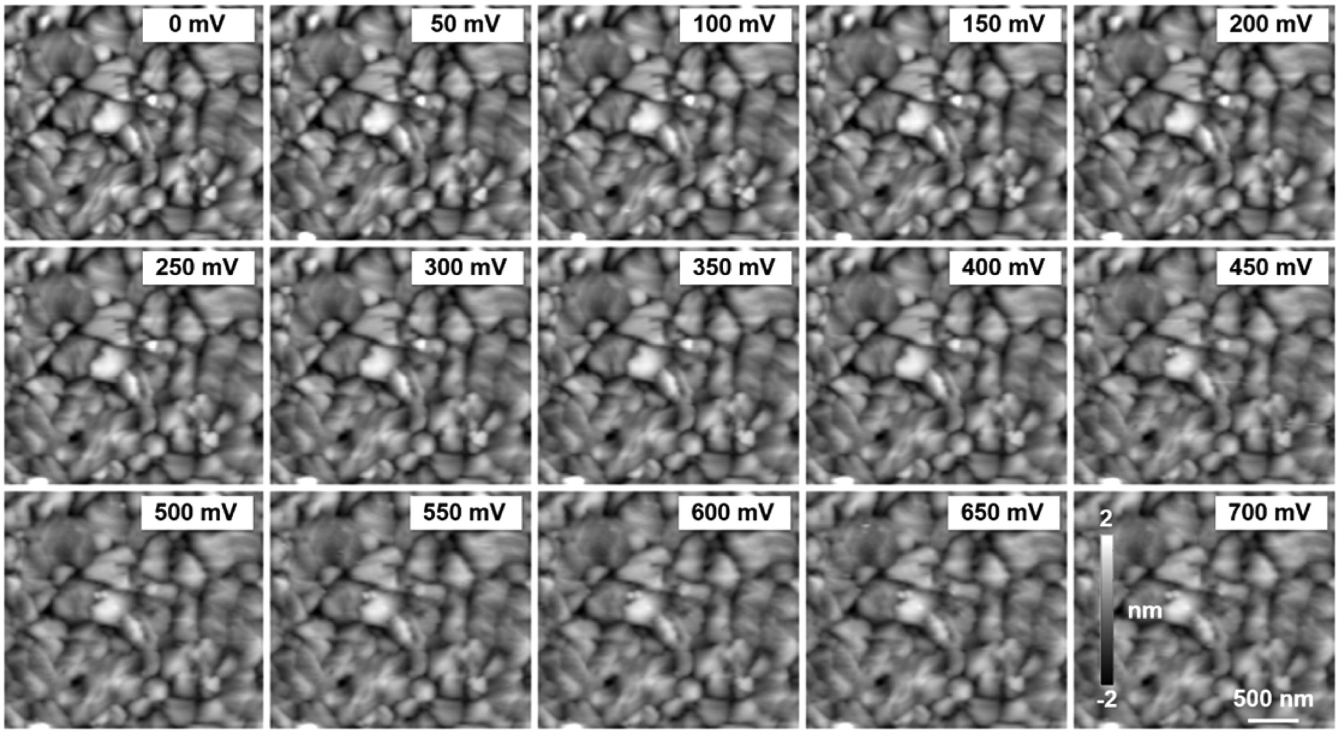

Figure 5. Montage of AFM height images of the $MAPbI_3$ thin film at different applied bias voltages as labeled throughout the photocurrent measurements during ~0.07 $W.cm^{-2}$ illumination, revealing negligible topographic damage throughout the ~2 h experiment.

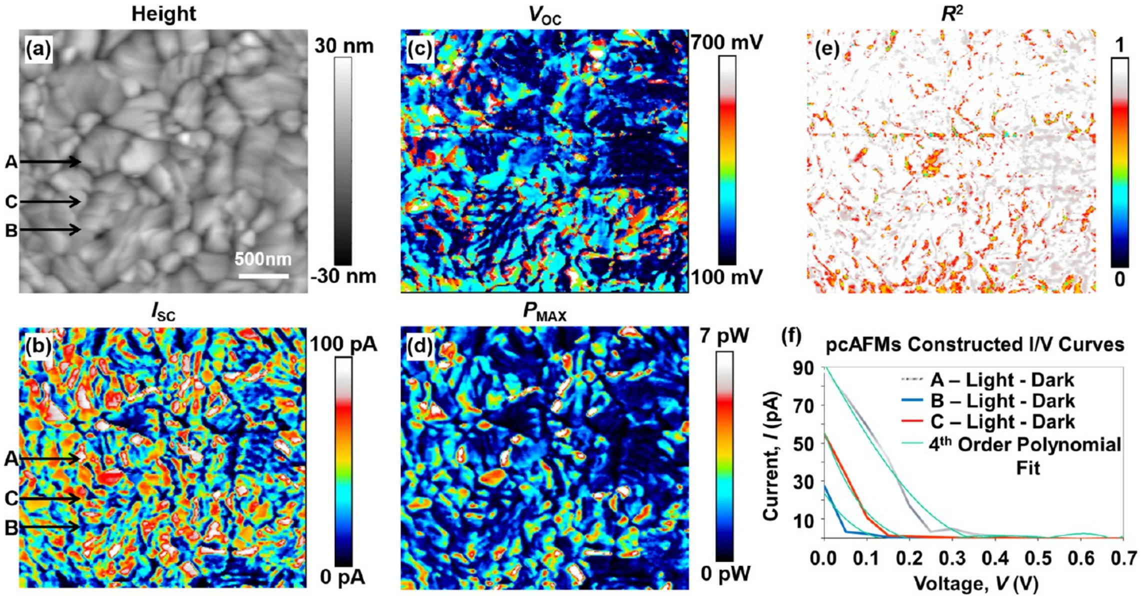

Figure 6. $MAPbI_3$ thin film: (a) topography (height), and pcAFMs resolved maps of (b) I_{SC}, (c) V_{OC}, and (d) P_{MAX} on a 2.86 μm × 2.61 μm area under ~0.07 $W.cm^{-2}$ illumination when the $MAPbI_3$ thin film is biased. (e) The R^2 correlation coefficient map provides the measure of the quality of the polynomial fitting of the $I-V$ data. (f) Three such $I-V$ curves and their fits are shown for representative spots A, B, and C, marked in (a) and (b) taken from 54 412 total spectra in this pcAFMs experiment.

128 min to collect all 30 images (256 lines per image, 1 Hz line rate always in the same direction to avoid any scan-direction inconsistencies). To better visualize the progression of the current response as the $MAPbI_3$ thin film locally approaches open-circuit conditions (typically 200−400 mV), the dark-corrected image contrast for the entire montage is displayed in a logarithmic scale representing 0.01−100 pA. A maximum photocurrent of 93 pA is detected for short circuit condition (0 mV), while beyond V_{OC} the current polarity becomes negative, as expected, but is not shown here because this is beyond the range of normal solar cell operation.

It is acknowledged that the measured photocurrents may diminish as a function of bias and/or imaging time due to unspecified damage either at the local position being probed or elsewhere along the 3D complex transport network. To address this concern, Figure 5 presents the simultaneously acquired surface topography for the 15 frames shown in Figure 4 (out of 30 total since every other image was acquired in dark

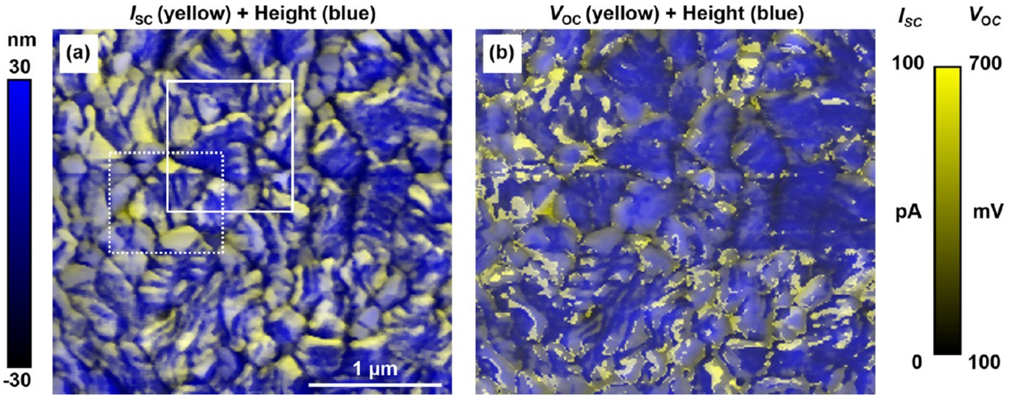

Figure 7. $MAPbI_3$ thin film topography (blue) overlaid with color contrast from pcAFMs resolved maps of (a) I_{SC} (yellow) and (b) V_{OC} (yellow) evidencing inter- and intragranular correlations between photovoltaic behavior and morphology.

conditions). There is no topographic damage except a barely visible smoothening. Specifically, the RMS roughness smoothly shifts from 8.98 to 8.48 nm (i.e., < 5.6%, across the entire montage), which is common in repeated AFM imaging and generally indicates gradual but minor surface and/or probe wear. Of course electrochemical reactions, electrical current-induced heat, or ambient exposure could cause additional effects, but such issues are usually accompanied by substantial changes in $MAPbI_3$ topography and the photovoltaic performance,[45,46] which clearly are not observed here.

Figure 6a redisplays the first topography image from Figure 5 (0 mV), alongside corresponding maps of I_{SC} (Figure 6b), V_{OC} (Figure 6c), and P_{MAX} (Figure 6d) for direct comparison. These maps of photoresponse parameters are calculated from Figure 4 by fitting the measured current (image contrast) versus applied voltage (image frame) with a fourth order polynomial at every image pixel in the pcAFMs data set. The correlation coefficient R^2 is also mapped (Figure 6e), evidencing reasonable fits. This approach provides up to 256 × 256 $I-V$ curves[22] for the 3 μm × 3 μm images acquired here. After cropping edge pixels that drifted out of the field-of-view as a result of inevitable but minor thermal drift during the experiment, this is reduced to 244 × 223 pixels (2.86 μm × 2.61 μm) of fully resolved $I-V$ spectra, and hence a total of 54 412 individual $I-V$ curves.

It is noteworthy that Figure 6 is based on data comparable to the conventionally acquired $I-V$ curves shown in Figure 3 but is more efficient and at nanoscale spatial resolution necessary for visualizing the fine spatial variations in the local photoresponse parameters of $MAPbI_3$ OTP thin film and other nanostructured PVs. For example, representative pcAFMs-based $I-V$ curves are shown from three different locations in Figure 6f, along with their corresponding fourth order polynomial fits. Of course, these curves are undersampled in the voltage domain compared to the point-by-point $I-V$ spectra presented in Figure 3 (by a factor of 8.8). Even higher fidelity $I-V$ data could be acquired with more images (i.e., smaller voltage increments). Sophisticated fitting/modeling schemes could also be implemented, the fourth order polynomial is selected out of convenience with qualitatively similar results for other fitting functions. However, the relatively smooth $I-V$ response measured at any given location, as opposed to the abrupt changes in photoresponse parameters for features with nanoscale separations (e.g., adjacent grains or grain boundaries), strongly justifies prioritizing spatial resolution over the number of voltage steps.

In terms of the somewhat depressed I/V curve shape and magnitude of V_{OC}, a thorough study into any effects of photodamage or light soaking may reveal a stronger and more “normal” response, because the experiments herein are performed with a rising bias over tens of minutes possibly leading to transient effects similar to those reported by Unger et al.[47] The rising voltage sweep was specifically selected to minimize any possible hysteresis effects. Comprehensive measurements are planned for the future, though, implementing rising and falling signals, forward and reverse biasing, and cycling, to investigate whether widely observed hysteresis effects[48−50] are homogeneous or localized. Measurements may be performed for a range of distinct tip types or coatings to vary the work function as well,[51] ideally even incorporating a sufficiently robust HTL layer directly on the probe to more completely approximate a full solar cell assembly. But the results presented herein demonstrate a reasonable balance of spatial resolution and functional mapping for these first nanoscale measurements of photoresponse parameters with PSCs.

Further analyzing the images in Figure 6 yields a mean I_{SC} of 38 pA, V_{OC} of 256 mV, and P_{MAX} of 2 pW with good fitting (R^2 > 0.90) over more than 70% of the image. Visually there appears to be a weak correlation between strong I_{SC} and high V_{OC}, while P_{MAX} essentially mirrors the I_{SC} contrast. Histograms of the I_{SC} and V_{OC} signals (Figure S2) also reveal that the top performing regions (e.g., the highest 50% of the measured values) again occupy a small areal fraction of the film, in this case 31% and 13% respectively.

Of course, these data cannot be directly compared with macroscopically measured PV performance parameters of $MAPbI_3$-based PSCs in the literature because those PSCs typically have a well-characterized contact area, a uniform HTL, and standardized measurements are performed under 1 sun ($0.1\ W.cm^{-2}$, simulated AM1.5G solar spectrum). Nevertheless, Figure 6 is telling as it exhibits both a highly granular photoresponse, as well as apparent grain-aggregates that are very photoactive and frequently observed to be adjacent to others with poor performance. This reveals grain and/or grain-aggregate localization of low-resistance current pathways, not just for I_{SC} conditions as demonstrated with Figures 2 and 3, but also throughout the power-generating $I-V$ quadrant.

Furthermore, the $MAPbI_3$ thin film topography (Figure 6a) reveals that most grains, especially larger ones, comprise regular striations aligned in distinct orientations within any given grain. Such microstructural features are often reported in $MAPbI_3$

OTP thin films.[7,8] The corresponding I_{SC} and V_{OC} maps, when overlaid as color contrast on height maps as in Figure 7a,b, respectively, often couples with these bandlike features. These are particularly clear in Figure S3a,b, which are magnified views of the regions sketched in Figure 7a. The frequently periodic, bandlike structures are hypothesized to represent either facets or the terminations of planar defects (twins, stacking faults) at the grain surfaces. The V_{OC} behavior does not appear to correlate as strongly with these striations as I_{SC} does, though many are visible in Figure 7b. While consistent variations in I_{SC} and V_{OC} at deep topographic crevices like some grain boundaries would evidence a common AFM artifact related to the contact area between the probe and the sample, the signals in fact are sometimes enhanced and sometimes diminished. This is especially clear when comparing topographic, I_{SC}, and V_{OC} line scans (Figure S3). Similar results have been reported with CdTe,[52] polycrystalline Si,[53] and PSCs as well.[54]

In closing, pcAFMs has been used to map for the first time the photoresponse for $MAPbI_3$ OTP thin films in terms of nanoscale versions of traditional PV performance parameters, I_{SC}, V_{OC}, and P_{MAX}. These results reveal substantial local variations in the photoresponse parameters of polycrystalline $MAPbI_3$ films that are hole-transport-layer free. Notably, in the case of I_{SC}, individual grains as well as aggregates of several adjacent grains exhibit similar values. Regions with the strongest I_{SC} and V_{OC}, of unknown origins but clearly coupled to microstructural features, also occupy less than 31% and 13% of the investigated area, respectively. The abrupt changes in the photoresponse parameters from one location to another strongly indicate that transport of photocarriers is promoted by high conductivity pathways (grains, interfaces), which are often disconnected from neighboring regions by other low-conductivity grains and interfaces acting as barriers. When transport is effectively unimpeded, photocarriers in $MAPbI_3$ thin films are demonstrated to exhibit sufficiently high mobilities and diffusion-lengths to cause uniform I_{SC} signals across as much as ~400 nm grains and/or grain-aggregates. Finally, linear features in the I_{SC} and V_{OC} contrast are often observed within individual grains likely due to the presence of planar defects (facets, twin boundaries, stacking faults, ferroelectric, or ferroelastic domains). Overall, these results highlight the importance of nanoscale investigations of the local PV performance for perovskite solar cells correlated to the microstructure of the organolead trihalide perovskites thin films. The unique insights gained from such studies are essential for guiding microstructural tailoring of OTP films for improved bulk PV performance in future PSCs.

■ ASSOCIATED CONTENT

Ⓢ Supporting Information

The Supporting Information is available free of charge on the ACS Publications website at DOI: 10.1021/acs.nanolett.5b04157.

> Histograms and cumulative histograms of the ISC images in dark and light conditions are illustrative of the areal fractions of low- and high-performing specimen regions, as well as the strong response to illumination. Histograms and cumulative histograms of ISC and VOC images similarly quantify the small areal fraction of high-performing specimen regions. High-magnification images and cross sections of topography, ISC, and VOC reveal sharp variations in these photovoltaic properties over length scales of tens of nanometers, generally uncorrelated with topography. (PDF)

■ AUTHOR INFORMATION

Corresponding Authors

*E-mail: nitin_padture@brown.edu (N.P.P.).
*E-mail: bryan.huey@uconn.edu (B.D.H.).

Notes

The authors declare no competing financial interest.

■ ACKNOWLEDGMENTS

The support for the work at Brown University from the National Science Foundation (DMR 1305913, OIA-1538893) is gratefully acknowledged. B.D.H. and Y.K. recognize the UConn Institute of Materials Science and support from DOE-BES-ESPM, Project DE-SC0005037.

■ REFERENCES

(1) Grätzel, M. *Nat. Mater.* **2014**, *13*, 838−842.
(2) Stranks, S. D.; Snaith, H. *Nat. Nanotechnol.* **2015**, *10*, 391−401.
(3) Kim, H.-S.; Lee, C.-R.; Im, J.-H.; Lee, K.-B.; Moehl, T.; Marchioro, A.; Moon, S.-J.; Humphry-Baker, R.; Yum, J.-H.; Moser, J. E.; Grätzel, M.; Park, N. G. *Sci. Rep.* **2012**, *2*, 591.
(4) Kojima, A.; Teshima, K.; Shirai, Y.; Miyasaka, T. *J. Am. Chem. Soc.* **2009**, *131*, 6050−6051.
(5) Yang, W. S.; Noh, J. H.; Jeon, N. J.; Kim, Y. C.; Ryu, S.; Seo, J.; Seok, S. I. *Science* **2015**, *348*, 1234−1237.
(6) Chen, Q.; Zhou, H.; Hong, Z.; Luo, S.; Duan, H.-S.; Wang, H.-H.; Liu, Y.; Li, G.; Yang, Y. J. *J. Am. Chem. Soc.* **2014**, *136*, 622−625.
(7) Yang, M.; Zhou, Y.; Zeng, Y.; Jiang, C. S.; Padture, N. P.; Zhu, K. *Adv. Mater.* **2015**, *27*, 6363−70.
(8) Zhou, Y.; Vasiliev, A. L.; Wu, W.; Yang, M.; Pang, S.; Zhu, K.; Padture, N. P. *J. Phys. Chem. Lett.* **2015**, *6*, 2292−2297.
(9) Conings, B.; Drijkoningen, J.; Gauquelin, N.; Babayigit, A.; D'Haen, J.; D'Olieslaeger, L.; Ethirajan, A.; Verbeeck, J.; Manca, J.; Mosconi, E.; Angelis, F. D.; Boyen, H. G. *Adv. Energy Mater.* **2015**, *5*, 1500477.
(10) Quarti, C.; Mosconi, E.; De Angelis, F. D. *Phys. Chem. Chem. Phys.* **2015**, *17*, 9394−9409.
(11) Zhao, Y.; Zhu, K. *J. Phys. Chem. Lett.* **2014**, *5*, 4175−4186.
(12) Huang, J.; Shao, Y.; Dong, Q. *J. Phys. Chem. Lett.* **2015**, *6*, 3218−3227.
(13) de Quilettes, D. W.; Vorpahl, S. M.; Stranks, S. D.; Nagaoka, H.; Eperon, G. E.; Ziffer, M. E.; Snaith, H. J.; Ginger, D. S. *Science* **2015**, *348*, 683−686.
(14) Xiao, M.; Huang, F.; Huang, W.; Dkhissi, Y.; Zhu, Y.; Etheridge, J.; Gray-Weale, A.; Bach, U.; Cheng, Y.-B.; Spiccia, L. *Angew. Chem.* **2014**, *126*, 10056−10061.
(15) Zhou, Y.; Yang, M.; Vasiliev, A. L.; Garces, H. F.; Zhao, Y.; Wang, D.; Pang, S.; Zhu, K.; Padture, N. P. *J. Mater. Chem. A* **2015**, *3*, 9249−9256.
(16) Jiang, C.-S.; Yang, M.; Zhou, Y.; To, B.; Nanayakkara, S.; Luther, J.; Zhou, W.; Berry, J.; van de Lagemaat, J.; Padture, N. P.; Zhu, K.; Al-Jassim, M. M. *Nat. Commun.* **2015**, *6*, 8397.
(17) Bergmann, V. W.; Weber, S. A. L. F.; Ramos, J.; Nazeeruddin, M. K.; Grätzel, M.; Li, D.; Domanski, A. L.; Lieberwirth, I.; Ahmad, S.; Berger, R. *Nat. Commun.* **2014**, *5*, 5001.
(18) Yun, J. S.; Ho-Baillie, A.; Huang, S.; Woo, S. H.; Heo, Y.; Seidel, J.; Huang, F.; Cheng, Y.-B.; Green, M. A. *J. Phys. Chem. Lett.* **2015**, *6*, 875−880.
(19) Kutes, Y.; Ye, L.; Zhou, Y.; Pang, S.; Huey, B. D.; Padture, N. P. *J. Phys. Chem. Lett.* **2014**, *5*, 3335−3339.
(20) Bosse, J. L.; Grishin, I.; Kolosov, O. V.; Huey, B. D. *J. Mater. Res.* **2013**, *28*, 3311−3321.

(21) Hamers, R. J.; Tromp, R. M.; Demuth, J. E. *Phys. Rev. Lett.* **1986**, *56*, 1972.

(22) Kutes, Y.; Aguirre, B. A.; Bosse, J. L.; Cruz-Campa, J. L.; Zubia, D.; Huey, B. D. *Prog. Photovoltaics* **2016**, *24*, 315−325.

(23) Zhou, Y.; Yang, M.; Wu, W.; Vasiliev, A. L.; Zhu, K.; Padture, N. P. *J. Mater. Chem. A* **2015**, *3*, 8178−8184.

(24) Zhou, Z.; Wang, Z.; Zhou, Y.; Pang, S.; Wang, D.; Xu, H.; Liu, Z.; Padture, N. P.; Cui, G. *Angew. Chem., Int. Ed.* **2015**, *54*, 9705−9709.

(25) Hu, H.; Wang, D.; Zhou, Y.; Zhang, J.; Lv, S.; Pang, S.; Chen, X.; Liu, Z.; Padture, N. P.; Cui, G. *RSC Adv.* **2014**, *4*, 28964−28967.

(26) Bi, C.; Wang, Q.; Shao, Y.; Yuan, Y.; Xiao, Z.; Huang, J. *Nat. Commun.* **2015**, *6*, 7747.

(27) Li, J. J.; Ma, J. Y.; Ge, Q. Q.; Hu, J. S.; Wang, D.; Wan, L. J. *ACS Appl. Mater. Interfaces* **2015**, *7*, 28518−28523.

(28) Kim, G. Y.; Oh, S. H.; Nguyen, B. P.; Jo, W.; Kim, B. J.; Lee, D. G.; Jung, H. S. *J. Phys. Chem. Lett.* **2015**, *6*, 2355−2362.

(29) Adhikari, N.; Dubey, A.; Khatiwada, D.; Mitul, A. F.; Wang, Q.; Venkatesan, S.; Iefanova, A.; Zai, J.; Qian, X.; Kumar, M.; Qiao, Q. *ACS Appl. Mater. Interfaces* **2015**, *7*, 26445−26454.

(30) Yun, J. S.; Ho-Baillie, A.; Huang, S.; Woo, S. H.; Heo, Y.; Seidel, J.; Huang, F.; Cheng, Y.-B.; Green, M. A. *J. Phys. Chem. Lett.* **2015**, *6*, 875−880.

(31) Yin, W. J.; Yang, J. H.; Kang, J.; Yan, Y.; Wei, S. H. *J. Mater. Chem. A* **2015**, *3*, 8926−8942.

(32) Beilsten-Edmands, J.; Eperon, G. E.; Johnson, R. D.; Snaith, H. J.; Radaelli, P. G. *Appl. Phys. Lett.* **2015**, *106*, 173502.

(33) Hermes, I. M.; Bretschneider, S. A.; Bergmann, V. W.; Li, D.; Klasen, A.; Mars, J.; Tremel, W.; Laquai, F.; Butt, H.-J.; Mezger, M.; Berger, R.; Rodriguez, B. J.; Weber, S. A. L. *J. Phys. Chem. C* **2016**, *120*, 5724−5731.

(34) Gruverman, A.; Auciello, O.; Tokumoto, H. *Annu. Rev. Mater. Sci.* **1998**, *28*, 101−123.

(35) Frost, J. M.; Butler, K. T.; Walsh, A. *APL Mater.* **2014**, *2*, 081506.

(36) Kim, H. S.; Kim, S. K.; Kim, B. J.; Shin, K. S.; Gupta, M. K.; Jung, H. S.; Kim, S. W.; Park, N. G. *J. Phys. Chem. Lett.* **2015**, *6*, 1729−1735.

(37) Liu, S.; Zheng, F.; Koocher, N. Z.; Takenaka, H.; Wang, F.; Rappe, A. M. *J. Phys. Chem. Lett.* **2015**, *6*, 693−699.

(38) Pecchia, A.; Gentilini, D.; Rossi, D.; Auf der Maur, M.; Di Carlo, A. *Nano Lett.* **2016**, *16*, 988−992.

(39) Xing, G.; Mathews, N.; Sun, S.; Lim, S. S.; Lam, Y. M.; Grätzel, M.; Mhaisalkar, S.; Sum, T. C. *Science* **2013**, *342*, 344−347.

(40) Stranks, S. D.; Eperon, G. E.; Grancini, G.; Menelaou, C.; Alcocer, M. J. P.; Leijtens, T.; Herz, L. M.; Petrozza, A.; Snaith, H. J. *Science* **2013**, *342*, 341−344.

(41) Oga, H.; Saeki, A.; Ogomi, Y.; Hayase, S.; Seki, S. *J. Am. Chem. Soc.* **2014**, *136*, 13818−13825.

(42) Ponseca, C. S., Jr.; Savenije, T. J.; Abdellah, M.; Zheng, K.; Yartsev, A.; Pascher, T.; Harlang, T.; Chabera, P.; Pullerits, T.; Stepanov, A.; Wolf, J.-P.; Sundstrom, V. *J. Am. Chem. Soc.* **2014**, *136*, 5189−5192.

(43) Marchioro, A.; Teuscher, J.; Friedrich, D.; Kunst, M.; Van De Krol, R.; Moehl, T.; Gratzel, M. *Nat. Photonics* **2014**, *8*, 250−255.

(44) Bi, C.; Wang, Q.; Shao, Y.; Yuan, Y.; Xiao, Z.; Huang, J. *Nat. Commun.* **2015**, *6*, 7747.

(45) Matsumoto, F.; Vorpahl, S. M.; Banks, J. Q.; Sengupta, E.; Ginger, D. S. *J. Phys. Chem. C* **2015**, *119*, 20810−20816.

(46) Tress, W.; Marinova, N.; Moehl, T.; Zakeeruddin, S. M.; Nazeeruddin, M. K.; Grätzel, M. *Energy Environ. Sci.* **2015**, *8*, 995−1004.

(47) Unger, E. L.; Hoke, E. T.; Bailie, C. D.; Nguyen, W. H.; Bowring, A. R.; Heumuller, T.; Christoforo, M. G.; McGehee, M. D. *Energy Environ. Sci.* **2014**, *7*, 3690−3698.

(48) Snaith, H. J.; Abate, A.; Ball, J. M.; Eperon, G. E.; Leijtens, T.; Noel, N. K.; Stranks, S. D.; Wang, J. T. W.; Wojciechowski, K.; Zhang, W. *J. Phys. Chem. Lett.* **2014**, *5*, 1511−1515.

(49) Brenner, T. M.; Egger, D. A.; Kronik, L.; Hodes, G.; Cahen, D. *Nat. Rev. Mater.* **2016**, *1*, 15007.

(50) Chen, B.; Yang, M.; Zheng, X.; Wu, C.; Li, W.; Yan, Y.; Bisquert, J.; Garcia-Belmonte, G.; Zhu, K.; Priya, S. *J. Phys. Chem. Lett.* **2015**, *6*, 4693−4700.

(51) Barnea-Nehoshtan, L.; Kirmayer, S.; Edri, E.; Hodes, G.; Cahen, D. *J. Phys. Chem. Lett.* **2014**, *5*, 2408−2413.

(52) Li, H.; Liu, X. X.; Lin, Y. S.; Yang, B.; Du, Z. M. *Phys. Chem. Chem. Phys.* **2015**, *17*, 11150−11155.

(53) Kazmerski, L. L.; Russell, P. E.; Ireland, P. J.; Herrington, C. R.; Dick, J. R.; Matson, R. J.; Jones, K. M. IEEE photovoltaics Specialists Conference, San Diego, CA, USA, 28 Sep 1982; Solar Energy Research Institute: Golden, CO, 1982.

(54) Docampo, P.; Hanusch, F. C.; Giesbrecht, N.; Angloher, P.; Ivanova, A.; Bein, T. *APL Mater.* **2014**, *2*, 081508.